Deterministic and efficient switching of sliding ferroelectrics

Shihan Deng [1,*] Hongyu Yu [1,*] Junyi Ji,[1] Changsong Xu,[1,2,†] and Hongjun Xiang [1,‡]
[1]*Key Laboratory of Computational Physical Sciences (Ministry of Education), Institute of Computational Physical Sciences, State Key Laboratory of Surface Physics, and Department of Physics, Fudan University, Shanghai 200433, China*
[2]*Hefei National Laboratory, Hefei 230088, China*

(Received 27 July 2024; accepted 4 April 2025; published 9 May 2025)

Recent studies highlight the scientific importance and broad application prospects of two-dimensional sliding ferroelectrics, which prevalently exhibit vertical polarization with suitable stackings. It is crucial to understand the mechanisms of sliding ferroelectricity and to deterministically and efficiently switch the polarization with optimized electric fields. Here, applying our DREAM-Allegro multitask equivariant neural network, which simultaneously predicts structure-dependent interatomic potentials and Born effective charges, we construct a comprehensive model for the boron nitride (BN) bilayer. The molecular dynamics simulations reveal a remarkably high Curie temperature of up to 1400 K, facilitated by robust intralayer chemical bonds and delicate interlayer van der Waals interactions. More importantly, it is found that, compared to the out-of-plane electric field, the inclined field not only leads to deterministic switching of electric polarization, but also largely lowers the critical strength of the field, due to the presence of the in-plane polarization in the transition state. This strategy of an inclined field is demonstrated to be universal for other sliding ferroelectric systems with monolayer structures belonging to the symmetry group $p\bar{6}m2$, such as transition metal dichalcogenides.

DOI: 10.1103/PhysRevB.111.174105

I. INTRODUCTION

Achieving ferroelectric devices with small thickness and perpendicular polarization is a critical step toward realizing low-energy, nonvolatile, and high-density ferroelectric memory. However, it is well known that the depolarization field becomes significant in thin-film ferroelectrics. Additionally, "dead layers" inevitably form due to factors such as interface effects, defects, and impurities, all of which lead to performance degradation in the application of ultrathin films [1,2].

The recently proposed concept of sliding ferroelectricity in two-dimensional (2D) van der Waals (vdW) materials naturally overcomes these obstacles [3]. The prototype of sliding ferroelectrics is the boron nitride (BN) bilayer [see Fig. 1(a)], which displays the energy ground state as the AB (BA) configuration [4–9] with C_{3v} symmetry. Within the AB configuration, the top B atom aligns with the bottom N atom, and the top N atom and the bottom B atom sit at the hollow sites of the honeycomb lattice. The AB (BA) stacking mode disrupts mirror symmetry and leads to an out-of-plane polarization of 2 pC/m in the $-z$ (z) direction [3,10]. This vertical polarization arises from charge redistribution driven by interlayer coupling [11–13]. The BA state can transition to the AB state via relative sliding between the two layers by a B-N bond length in any of the three rotationally symmetric directions [10,13,14]. Conversely, sliding in the opposite direction by one bond length leads to the mirror-symmetric (D_{3h}) AA state, representing the highest-energy state. Sliding ferroelectrics, especially the proposal of bilayer stacking ferroelectricity (BSF) theory [15], broadens the spectrum of candidate materials for 2D ferroelectrics, as bilayers made of nonpolar monolayers can exhibit ferroelectricity through specific stackings. Beyond the BN bilayer, sliding ferroelectrics has been experimentally confirmed in various vdW systems, including semimetals [16–20], insulators [21], semiconductors [22–26], and organic crystals [27], all of which are robust at room temperature. Notably, recent experiments highlighting high endurance and fatigue resistance in sliding ferroelectrics underscore the significant potential of these materials for practical applications [28,29].

The study of sliding ferroelectricity is rapidly developing, with both fundamental and practical challenges yet to be addressed. Although the switching energy barriers are typically very low (∼meV per unit cell [3,30,31]), sliding ferroelectrics exhibit high Curie temperatures (T_C). The underlying mechanism is still not clear and the T_C obtained through thermodynamic modeling using a mean-field approximation is excessively high, with a value of 1.58×10^4 K for the BN bilayer [14]. Additionally, the polarization of sliding ferroelectrics is typically small, leading to a large coercive field for polarization switching, which indicates that a wiser and more efficient switching strategy is highly desired. *Ab initio* molecular dynamics (AIMD) can be used to study sliding ferroelectricity, but it cannot handle large systems and is computationally consuming [32]. Moreover, symmetry changes during sliding, indicating that the Born effective charges (BECs) can change dramatically [33] [see Fig. S1 in the Supplemental Material (SM) [34] (including Refs. [10,24,35–51]) for the sliding-related BEC components of the BN bilayer along the sliding pathway], and the treatment with fixed BEC will be insufficient [52] (see Sec. SI in SM for a detailed

*These authors contributed equally to this work.
†Contact author: csxu@fudan.edu.cn
‡Contact author: hxiang@fudan.edu.cn

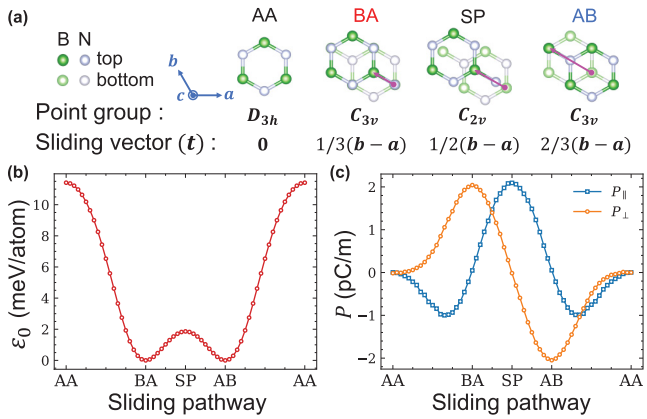

FIG. 1. (a) Schemes of the AA, BA, AB, and SP stackings of the BN bilayer. Blue arrows define the lattice vectors $\boldsymbol{a}$, $\boldsymbol{b}$, and $\boldsymbol{c}$ of the unit cell. Purple arrows indicate possible sliding vectors $\boldsymbol{t}$. (b) Energy ε_0 and (c) polarization $\boldsymbol{P}$ along the sliding pathway, as calculated by the DFT and the Berry phase approach [53,54].

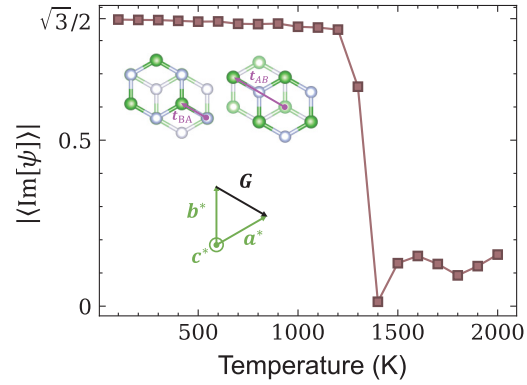

FIG. 2. $|\langle \mathrm{Im}[\psi] \rangle| = |\langle \sin(\mathbf{G} \cdot \mathbf{t}) \rangle|$ at varying temperatures. Green arrows denote the reciprocal lattice vectors $\boldsymbol{a}^*$ and $\boldsymbol{b}^*$, and the black arrow indicates that $\boldsymbol{G} = \boldsymbol{a}^* - \boldsymbol{b}^*$ is selected. Purple arrows visualize a possible sliding vector $\boldsymbol{t}$ of the BA and AB state, which are $\boldsymbol{t}_{\mathrm{BA}} = 1/3(\boldsymbol{b} - \boldsymbol{a})$ and $\boldsymbol{t}_{\mathrm{AB}} = 2/3(\boldsymbol{b} - \boldsymbol{a})$, respectively.

discussion [34]). Hence, an accurate and efficient description of sliding ferroelectric systems is required.

In this article, applying our DREAM method (i.e., a generalized dielectric response equivariant atomistic multitask framework based on Allegro [45]), we construct a neural network model for the BN bilayer. Such a model is capable of predicting both the interatomic potential and the BEC tensors for a given structure, which enables the prediction of a reasonable T_C and accurate responses to applied electric fields. Moreover, it is found that an inclined electric field, which breaks the threefold rotational symmetry of the BN bilayer, can not only deterministically control the directions of sliding, but also substantially reduces the total coercive field. These findings are general and can be applied to other similar sliding ferroelectrics.

II. FERROELECTRIC TRANSITION IN THE BN BILAYER

First, the basic properties of the BN bilayer are examined by density functional theory (DFT) calculations. As illustrated in Figs. 1(b) and 1(c), the out-of-plane polarization ($P_\perp$) of the AB (BA) state yields ∓ 2.078 pC/m, and the energy barrier for polarization switching is determined to be 7.44 meV per unit cell. Such results are well consistent with those of previous studies [3,10]. Notably, the transition state or intermediate saddle-point (SP) state with C_{2v} symmetry exhibits a strictly in-plane polarization ($P_\parallel$) of 2.091 pC/m. The presence of $P_\parallel$ has been derived from BSF theory in Ref. [15], and also corroborated by other theoretical calculations [55–57] as well as experimental findings [58].

In order to train the potential model using the original Allegro method [45], we employ AIMD in conjunction with on-the-fly machine learning force fields (MLFFs) [40–42]. This approach allows us to sample structures more efficiently as training datasets. The molecular dynamics (MD) simulations are conducted in a $5 \times 5 \times 1$ supercell across a broad temperature range up to 3000 K. From these simulations, we extract a total of 1659 structures, using their energies, forces, and stress tensors for model training. The obtained model can accurately predict the energy difference among different structures, with a small mean absolute errors (MAEs) of 0.053 meV/atom (see Sec. SII in SM for more information about computational details and model accuracy).

In the case of sliding ferroelectricity, T_C can be characterized by the sliding vector $\boldsymbol{t}$ [14],

$$\lim_{T \to T_C^-} \frac{\partial \langle \|\boldsymbol{t}\| \rangle}{\partial T} \to \infty, \tag{1}$$

where $\langle\ \rangle$ signifies the ensemble average at a certain temperature. Sliding vector $\boldsymbol{t}$ can be defined as the averaged displacements of the top layer with respect to the bottom layer starting from the AA stacking [see Fig. 1(a)]. To circumvent artifacts from periodic lattice effects, we use the reciprocal lattice vector ($\boldsymbol{G}$) to define a new order parameter (ψ), which reads

$$\psi(\boldsymbol{t}) = e^{i\boldsymbol{G}\cdot\boldsymbol{t}}. \tag{2}$$

ψ remains unchanged under lattice translation $\boldsymbol{t} \to \boldsymbol{t} + \boldsymbol{R}$, where $\boldsymbol{R}$ represents the in-plane lattice vector.

We now investigate the ferroelectric-paraelectric phase transition in the BN bilayer through MD simulations. Using our developed potential model, we perform thermal equilibration simulations at 100 K intervals across the 100–2000 K temperature range, maintaining 900 atoms in each simulation. The order parameter ψ is subsequently calculated from 1 nanosecond (ns) equilibrium trajectories. Figure 2 displays the temperature dependence of $|\langle \mathrm{Im}[\psi] \rangle|$ for $\boldsymbol{G} = \boldsymbol{a}^* - \boldsymbol{b}^*$, obtained from two independent parallel simulations. The phase transition occurs at $T_C \approx 1400$ K: Below this temperature, the system preserves ferroelectric order with $\mathrm{Im}[\psi_{\mathrm{BA}}] = \sqrt{3}/2$ or $\mathrm{Im}[\psi_{\mathrm{AB}}] = -\sqrt{3}/2$, corresponding to the BA and AB stacking configurations, respectively. Thermal fluctuations above T_C induce interlayer sliding that completely suppresses the polar order. This predicted transition temperature shows striking improvement over the mean-field approximation result of 1.58×10^4 K [14]. Notably, the minimal variation in the intralayer B-N bond lengths during sliding reveals that robust intralayer covalent interactions, rather than interlayer effects,

dominate the exceptional thermal stability of polarization in this sliding ferroelectric system.

III. SWITCHING OF SLIDING FERROELECTRICITY IN THE BN BILAYER

To simulate the BN bilayer under an external electric field, we integrate Allegro within the new DREAM framework [46], as implemented in PASP [59]. This integration enables the network to learn both scalars and tensors by leveraging geometric tensors [60,61]. Consequently, the network is capable of simultaneously predicting structure-dependent interatomic potentials and BECs. The dataset incorporates BEC information of 3484 structures sampled at temperatures below 500 K, and the MAEs of the final model yields 0.030 meV/atom in energy and 0.008 $|e|$ in BEC, demonstrating good accuracy of the model (see Sec. SII in SM for more information about training details and model accuracy). The parity plot and MAE distributions of energy and BEC are shown in Fig. S2 [34].

We now examine the responses of the BN bilayer to perpendicular field $E_\perp$. We start with the ferroelectric BA state and incrementally increase $E_\perp$ along the $-z$ direction over time at a rate of 0.02 V/(Å ps), at temperatures ranging from 100 to 500 K. The sliding process is brief, typically completed within a few picoseconds. We identify the coercive field ($E_{\perp,c}$) as the field at which sliding reaches the SP state, since thermal vibrations add difficulty to identifying the exact onset of sliding. Our results indicate that $E_{\perp,c}$ decreases with increasing temperature, starting at approximately 1.99 V/Å at 100 K and saturating at around 1.39 V/Å for over 200 K [see the orange line in Fig. 4(a)]. Moreover, since $E_\perp$ does not break the threefold rotational symmetry of the BN bilayer, sliding occurs randomly along the three rotationally symmetric directions in each simulation [see the top panel of Fig. 3(b)].

Given that some sliding states of the BN bilayer exhibit $P_\parallel$, we investigate the effect of in-plane electric field ($E_\parallel$) on ferroelectric switching. As revealed by Fig. 3(a), the direction of $P_\parallel$ is the same as the corresponding sliding direction, which can be characterized by the angle θ (measured through a counterclockwise rotation from the y axis). This finding implies that $E_\parallel$ oriented along one of these three directions can break the threefold rotational symmetry and induce deterministic switching. For instance, $E_\parallel$ oriented at 60° will lead to sliding being only along 60° [see the lower panel of Fig. 3(b)]. Actually, applying $E_\parallel$ within the range of (0°, 120°) can all lead to sliding along 60°, with $E_\parallel$ along 60° being the most efficient (see MD results in Fig. S5). In addition, Fig. 3(a) shows significant $P_\parallel$ at the bridging SP state, which indicates that suitable $E_\parallel$ can substantially reduce the energy barrier. Such a conjecture can be verified by the energy distribution shown in the first two columns of Fig. 3(c), where the energy barrier for sliding from the BA to AB state is obviously reduced in the presence of $E_\parallel$.

Moreover, the decrease in the energy barriers also indicates that the presence of $E_\parallel$ may reduce $E_{\perp,c}$. To examine such a conjecture, we fit the energy ε_0, in-plane dipole $p_\parallel$, and out-of-plane dipole $p_\perp$ as a function of the distance of sliding (t) with respect to the SP state, i.e., $t_{\mathrm{SP}} = 0$, along the BA to AB sliding pathway. The fitted models yield

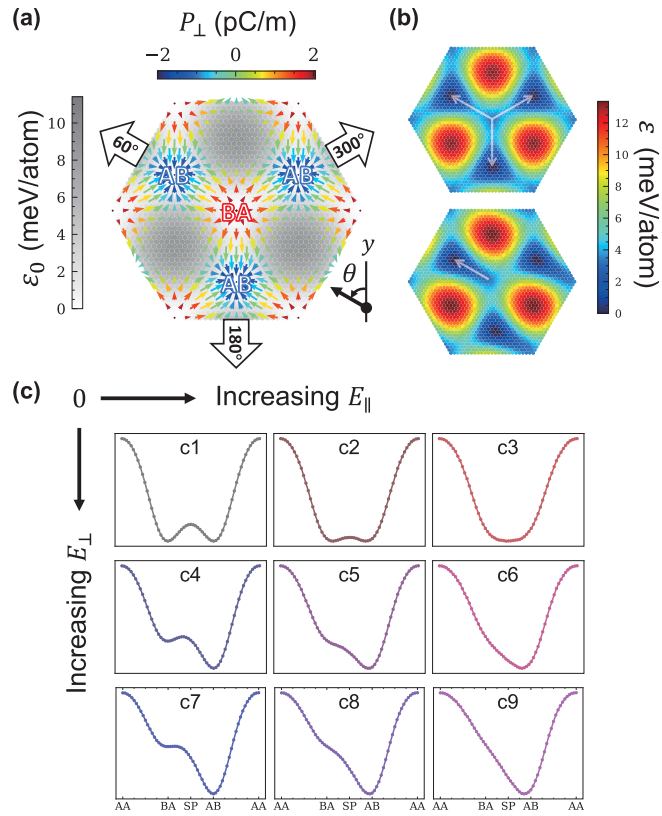

FIG. 3. (a) Energy ε_0 and polarization P distribution calculated by the DFT and the Berry phase approach. Positions within the hexagon correspond to different sliding vectors, with the center representing the BA state. The varying shades of gray in the background represent the levels of energy. The length and direction of colored arrows show in-plane polarizations $P_\parallel$, while their colors represent out-of-plane polarization $P_\perp$. The sliding directions θ are indicated by large open arrows. (b) The energy surface with only $E_\perp$ along $-z$ (the top panel) and with both $E_\perp$ along $-z$ and $E_\parallel$ at 60° (the bottom panel), calculated according to Eq. (3) with $E_\perp$ and $E_\parallel$ equal to 1 V/Å. White arrows denote the sliding pathways with the lowest barrier. (c) Energy along the sliding pathway under varying $E_\parallel$ and $E_\perp$, also calculated using Eq. (3). $E_\parallel$ gradually increases from the left to right panels, and $E_\perp$ gradually increases from the top to bottom panels.

$\varepsilon_0(t) = e_4 t^4 - 2e_4 t_{\mathrm{BA}}^2 t^2 + e_0$, $p_\parallel(t) = p_4^\parallel t^4 + p_2^\parallel t^2 - p_4^\parallel t_{\mathrm{BA}}^4 - p_2^\parallel t_{\mathrm{BA}}^2$, and $p_\perp(t) = p_3^\perp t^3 - 3p_3^\perp t_{\mathrm{BA}}^2 t$, where $t_{\mathrm{BA}} = -1/6|\boldsymbol{b} - \boldsymbol{a}| = -0.725$ Å is a constant. The fitting plots are shown in Fig. S3, and the coefficients are determined to be $e_4 = 27.017$ meV/Å^4, $e_0 = 7.41$ meV, $p_4^\parallel = 5.82 \times 10^{-3} e$/Å^3, $p_2^\parallel = -16.56 \times 10^{-3} e$/Å, and $p_3^\perp = 9.13 \times 10^{-3} e$/Å^2. The total potential energy after applying $E_\parallel$ along the BA to AB sliding direction and $E_\perp$ can then be expressed as

$$\varepsilon(t) = \varepsilon_0(t) - E_\parallel \cdot p_\parallel(t) - E_\perp \cdot p_\perp(t). \tag{3}$$

If we define the critical field as the minimum field at which the local energy minimum of $\varepsilon(t)$ disappears, i.e., $\mathrm{d}\varepsilon(t)/\mathrm{d}t \leqslant 0$, along the BA to SP sliding pathway [see the top inset of Fig. 4(b)], then $E_{\perp,c}$ along $-z$ can be obtained analytically for a given $E_\parallel$ by solving Eq. (3) [see the purple line in Fig. 4(b)]. The detailed derivation and the complete analytical

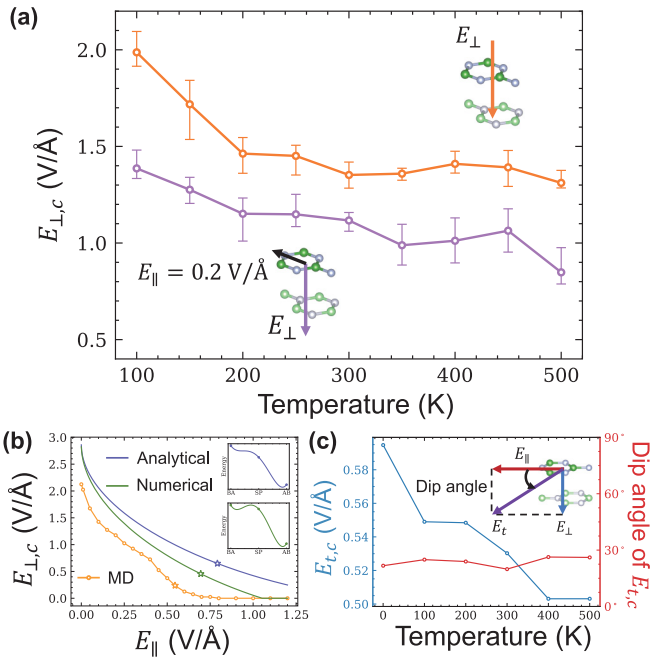

FIG. 4. (a) $E_{\perp,c}$ at varying temperatures. The orange and purple lines represent the scenarios with $E_\parallel = 0$ and $E_\parallel = 0.2$ V/Å at $\theta = 60^\circ$, respectively. The error bars indicate the range of results from parallel simulations. (b) The relationship between $E_{\perp,c}$ and $E_\parallel$, as obtained by analytical calculations (purple line), numerical calculations (green line), and MD simulations at 0.1 K (yellow line). The pentagram marks on the curves indicate the minimum $E_{t,c}$. The insets depict the energy along the sliding pathway with the minimum $E_{t,c}$ obtained by analytical (the top panel) and numerical (the bottom panel) calculations, respectively. (c) The magnitude (blue line) and dip angle (red line) of the minimum $E_{t,c}$ across different temperatures. The dip angle is defined as the angle between $E_{t,c}$ and the horizontal plane.

expression of $E_{\perp,c}$ are provided in Sec. SIII in SM. When $E_\parallel < 1$ V/Å, $E_{\perp,c}$ can be approximatively expressed in terms of $\sqrt{E_\parallel}$ as

$$E_{\perp,c} = -\frac{4e_4 t_{\mathrm{BA}}}{3p_3^\perp}\left(1 - \sqrt{-\frac{p_2^\parallel + 2p_4^\parallel t_{\mathrm{BA}}^2}{e_4 t_{\mathrm{BA}}^2}}\sqrt{E_\parallel}\right) \equiv E_{\perp,c}^0(1 - \beta\sqrt{E_\parallel}), \tag{4}$$

where $\beta > 0$ (see Fig. S4 for the good approximation accuracy). Clearly, Eq. (4) shows that the presence of $E_\parallel$ will reduce the required $E_{\perp,c}$. In the absence of $E_\parallel$, $E_{\perp,c}^0 = -4e_4 t_{\mathrm{BA}}/3p_3^\perp = 2.86$ V/Å is the purely vertical coercive field. More importantly, it is further found that the presence of $E_\parallel$ can lower the total coercive field $E_{t,c}$. When $E_\parallel \to 0$, $E_{t,c}$ can be expressed as

$$E_{t,c} = \sqrt{(E_{\perp,c})^2 + (E_\parallel)^2} \to E_{\perp,c}^0(1 - \beta\sqrt{E_\parallel}) < E_{\perp,c}^0, \tag{5}$$

which clearly demonstrates that $E_{t,c}$ is smaller than $E_{\perp,c}^0$ with infinitesimal $E_\parallel$. Alternatively, if we define the critical field as the minimum field such that $\varepsilon(t)$ does not exceed the energy of the BA state, i.e., $\varepsilon(t) \leqslant \varepsilon(t_{\mathrm{BA}})$ [see the bottom inset of Fig. 4(b)], $E_{\perp,c}$ can also be solved numerically for a given $E_\parallel$, as shown by the green line in Fig. 4(b). In both analytical and numerical cases, the minimum $E_{t,c}$ is reduced by more than 64% and 70%, respectively, comparing to the $E_{\perp,c}^0$.

Then, we conduct MD simulations to verify the prediction that finite $E_\parallel$ can lower $E_{\perp,c}$ and $E_{t,c}$. By applying a constant $E_\parallel$ of 0.2 V/Å along the $\theta = 60^\circ$ direction, $E_{\perp,c}$ is found to significantly reduce, compared to $E_\parallel = 0$ [see Fig. 4(a)]. As in the previous analysis, this adjustment ensures that sliding occurred exclusively at $\theta = 60^\circ$. However, insufficient $E_\parallel$ strength may not adequately counteract random thermal fluctuations, potentially resulting in alternative sliding directions.

To determine the configurations of $E_{t,c}$ necessary to initiate sliding, we apply an inclined electric field to the BN bilayer at different temperatures. The field has varying in-plane and vertical components, adjusted in increments of 0.05 V/Å. The configurations of $E_{t,c}$ that initiate sliding within 30 ps at different temperatures are depicted in Fig. S6. The curve at 0.1 K is also represented by the yellow line in Fig. 4(b), exhibiting a trend consistent with previous theoretical analyses. As shown in Fig. 4(c), the minimum $E_{t,c}$ decreases by over 70% as the temperature decreases, compared to the purely vertical $E_{t,c}$ in Fig. 4(a). It is noteworthy that experimentally measured coercive fields are often significantly lower than theoretically predicted values. This discrepancy, potentially related to the Landauer paradox [62–64], may be due to the presence of inhomogeneities in the experimental samples [65,66]. Furthermore, the presence of domain walls may also significantly reduce coercive fields [67]. On another aspect, the dip angle of the minimum $E_{t,c}$ at different temperatures almost remains constant at 24°. Such constant behavior will benefit experimental setups and also device design.

IV. DISCUSSION

The decrease in $E_{t,c}$ with applying an inclined electric field relies on the presence of in-plane polarization along the sliding pathway. According to a symmetry analysis [15], parallel-stacked bilayers, which are made of monolayers with the same space group of $p\bar{6}m2$ as BN, all display the required in-plane polarization. Such a discovery indicates that the strategy of the inclined field can be generalized to different sliding systems, such as the widely studied transition metal dichalcogenides (TMDs) WSe_2, $MoSe_2$, WS_2, and MoS_2 [24,25,29], as well as InSe [22,23]. To confirm this prediction, we verify the energy and polarization distribution of MoS_2 (see Fig. S7 [34]), which differs from BN only in the opposite direction of in-plane polarization. Hence, the direction of $E_\parallel$ needs to be reversed to achieve efficient switching.

In conclusion, our machine-learning-assisted DREAM-Allegro model effectively predicts the structure-dependent interatomic energy and BECs of a parallel-stacked BN bilayer. This enables accurate prediction of the temperature and field effects by performing MD simulations. Applying both simulations and theoretical analyses, we find that the in-plane field can lead to the deterministic switching of polarization and an inclined field can largely reduce the critical field required for switching. Such a strategy is further generated to widely studied sliding ferroelectrics and thus paves the way for applications.

ACKNOWLEDGMENTS

We acknowledge financial support from the National Key R&D Program of China (Grant No. 2022YFA1402901), NSFC (Grants No. 12188101, No. 12174060, and No. 12274082), the Guangdong Major Project of the Basic and Applied Basic Research (Future functional materials under extreme conditions–2021B0301030005), Shanghai Science and Technology Program (Grant No. 23JC1400900), and Shanghai Pilot Program for Basic Research–FuDan University 21TQ1400100 (23TQ017). C.X. also acknowledges support from the Shanghai Science and Technology Committee (Grant No. 23ZR1406600), Shanghai Education Committee (Grant No. 24KXZNA01), Innovation Program for Quantum Science and Technology (Grant No. 2024ZD0300102), and the Xiaomi Young Talents Program.

[1] J. Müller, P. Polakowski, S. Mueller, and T. Mikolajick, Ferroelectric hafnium oxide based materials and devices: Assessment of current status and future prospects, ECS J. Solid State Sci. Technol. **4**, N30 (2015).

[2] M. Stengel and N. A. Spaldin, Origin of the dielectric dead layer in nanoscale capacitors, Nature (London) **443**, 679 (2006).

[3] L. Li and M. Wu, Binary compound bilayer and multilayer with vertical polarizations: Two-dimensional ferroelectrics, multiferroics, and nanogenerators, ACS Nano **11**, 6382 (2017).

[4] R. M. Ribeiro and N. M. R. Peres, Stability of boron nitride bilayers: Ground-state energies, interlayer distances, and tight-binding description, Phys. Rev. B **83**, 235312 (2011).

[5] M. V. Stern, Y. Waschitz, W. Cao, I. Nevo, K. Watanabe, T. Taniguchi, E. Sela, M. Urbakh, O. Hod, and M. B. Shalom, Interfacial ferroelectricity by van der Waals sliding, Science **372**, 1462 (2021).

[6] K. Yasuda, X. Wang, K. Watanabe, T. Taniguchi, and P. Jarillo-Herrero, Stacking-engineered ferroelectricity in bilayer boron nitride, Science **372**, 1458 (2021).

[7] M. Wu and J. Li, Sliding ferroelectricity in 2D van der Waals materials: Related physics and future opportunities, Proc. Natl. Acad. Sci. USA **118**, e2115703118 (2021).

[8] G. Constantinescu, A. Kuc, and T. Heine, Stacking in bulk and bilayer hexagonal boron nitride, Phys. Rev. Lett. **111**, 036104 (2013).

[9] E. Y. Tsymbal, Two-dimensional ferroelectricity by design, Science **372**, 1389 (2021).

[10] W. Jiang, C. Liu, X. Ma, X. Yu, S. Hu, X. Li, L. A. Burton, Y. Liu, Y. Chen, P. Guo, X. Kong, L. Bellaiche, and W. Ren, Anomalous ferroelectricity and double-negative effects in bilayer hexagonal boron nitride, Phys. Rev. B **106**, 054104 (2022).

[11] Z. Zheng, Q. Ma, Z. Bi, S. de la Barrera, M.-H. Liu, N. Mao, Y. Zhang, N. Kiper, K. Watanabe, T. Taniguchi, J. Kong, W. A. Tisdale, R. Ashoori, N. Gedik, L. Fu, S.-Y. Xu, and P. Jarillo-Herrero, Unconventional ferroelectricity in moiré heterostructures, Nature (London) **588**, 71 (2020).

[12] C. Wang, L. You, D. Cobden, and J. Wang, Towards two-dimensional van der Waals ferroelectrics, Nat. Mater. **22**, 542 (2023).

[13] M. Liu, H. Ji, Z. Fu, Y. Wang, J.-T. Sun, and H.-J. Gao, Orbital distortion and electric field control of sliding ferroelectricity in a boron nitride bilayer, J. Phys.: Condens. Matter **35**, 235001 (2023).

[14] P. Tang and G. E. W. Bauer, Sliding phase transition in ferroelectric van der Waals bilayers, Phys. Rev. Lett. **130**, 176801 (2023).

[15] J. Ji, G. Yu, C. Xu, and H. J. Xiang, General theory for bilayer stacking ferroelectricity, Phys. Rev. Lett. **130**, 146801 (2023).

[16] Z. Fei, W. Zhao, T. A. Palomaki, B. Sun, M. K. Miller, Z. Zhao, J. Yan, X. Xu, and D. H. Cobden, Ferroelectric switching of a two-dimensional metal, Nature (London) **560**, 336 (2018).

[17] P. Sharma, F.-X. Xiang, D.-F. Shao, D. Zhang, E. Y. Tsymbal, A. R. Hamilton, and J. Seidel, A room-temperature ferroelectric semimetal, Sci. Adv. **5**, eaax5080 (2019).

[18] J. Xiao, Y. Wang, H. Wang, C. D. Pemmaraju, S. Wang, P. Muscher, E. J. Sie, C. M. Nyby, T. P. Devereaux, X. Qian, X. Zhang, and A. M. Lindenberg, Berry curvature memory through electrically driven stacking transitions, Nat. Phys. **16**, 1028 (2020).

[19] S. C. de la Barrera, Q. Cao, Y. Gao, Y. Gao, V. S. Bheemarasetty, J. Yan, D. G. Mandrus, W. Zhu, D. Xiao, and B. M. Hunt, Direct measurement of ferroelectric polarization in a tunable semimetal, Nat. Commun. **12**, 5298 (2021).

[20] A. Jindal, A. Saha, Z. Li, T. Taniguchi, K. Watanabe, J. C. Hone, T. Birol, R. M. Fernandes, C. R. Dean, A. N. Pasupathy, and D. A. Rhodes, Coupled ferroelectricity and superconductivity in bilayer T_d-$MoTe_2$, Nature (London) **613**, 48 (2023).

[21] M. Lv, X. Sun, Y. Chen, T. Taniguchi, K. Watanabe, M. Wu, J. Wang, and J. Xue, Spatially resolved polarization manipulation of ferroelectricity in twisted hBN, Adv. Mater. **34**, 2203990 (2022).

[22] H. Hu, Y. Sun, M. Chai, D. Xie, J. Ma, and H. Zhu, Room-temperature out-of-plane and in-plane ferroelectricity of two-dimensional β-InSe nanoflakes, Appl. Phys. Lett. **114**, 252903 (2019).

[23] F. Sui, M. Jin, Y. Zhang, R. Qi, Y.-N. Wu, R. Huang, F. Yue, and J. Chu, Sliding ferroelectricity in van der Waals layered γ-InSe semiconductor, Nat. Commun. **14**, 36 (2023).

[24] X. Wang, K. Yasuda, Y. Zhang, S. Liu, K. Watanabe, T. Taniguchi, J. Hone, L. Fu, and P. Jarillo-Herrero, Interfacial ferroelectricity in rhombohedral-stacked bilayer transition metal dichalcogenides, Nat. Nanotechnol. **17**, 367 (2022).

[25] Y. Sun, S. Xu, Z. Xu, J. Tian, M. Bai, Z. Qi, Y. Niu, H. H. Aung, X. Xiong, J. Han, C. Lu, J. Yin, S. Wang, Q. Chen, R. Tenne, A. Zak, and Y. Guo, Mesoscopic sliding ferroelectricity enabled photovoltaic random access memory for material-level artificial vision system, Nat. Commun. **13**, 5391 (2022).

[26] Y. Wan, T. Hu, X. Mao, J. Fu, K. Yuan, Y. Song, X. Gan, X. Xu, M. Xue, X. Cheng, C. Huang, J. Yang, L. Dai, H. Zeng, and E. Kan, Room-temperature ferroelectricity in 1T′-ReS_2 multilayers, Phys. Rev. Lett. **128**, 067601 (2022).

[27] L.-P. Miao, N. Ding, N. Wang, C. Shi, H.-Y. Ye, L. Li, Y.-F. Yao, S. Dong, and Y. Zhang, Direct observation of geometric and sliding ferroelectricity in an amphidynamic crystal, Nat. Mater. **21**, 1158 (2022).

[28] K. Yasuda, E. Zalys-Geller, X. Wang, D. Bennett, S. S. Cheema, K. Watanabe, T. Taniguchi, E. Kaxiras, P. Jarillo-Herrero, and

R. Ashoori, Ultrafast high-endurance memory based on sliding ferroelectrics, Science **385**, 53 (2024).

[29] R. Bian, R. He, E. Pan, Z. Li, G. Cao, P. Meng, J. Chen, Q. Liu, Z. Zhong, W. Li, and F. Liu, Developing fatigue-resistant ferroelectrics using interlayer sliding switching, Science **385**, 57 (2024).

[30] Q. Yang, M. Wu, and J. Li, Origin of two-dimensional vertical ferroelectricity in WTe_2 bilayer and multilayer, J. Phys. Chem. Lett. **9**, 7160 (2018).

[31] M. Wu, Two-dimensional van der Waals ferroelectrics: Scientific and technological opportunities, ACS Nano **15**, 9229 (2021).

[32] B. Shi, H. Wang, W. Jiang, Y. Feng, P. Guo, H. Gao, Z. Gao, and W. Ren, Electric field effect of sliding graphene/hexagonal boron nitride heterobilayer, Appl. Surf. Sci. **636**, 157816 (2023).

[33] D. Bennett and P. Ghosez, Asymmetric dynamical charges in two-dimensional ferroelectrics, Phys. Rev. B **110**, L041101 (2024).

[34] See Supplemental Material at http://link.aps.org/supplemental/10.1103/PhysRevB.111.174105 for Born effective charges of the BN bilayer, computational details, model accuracy, analytical and numerical calculation of the coercive electric field, and supplemental figures.

[35] G. Kresse and J. Furthmüller, Efficient iterative schemes for *ab initio* total-energy calculations using a plane-wave basis set, Phys. Rev. B **54**, 11169 (1996).

[36] P. E. Blöchl, Projector augmented-wave method, Phys. Rev. B **50**, 17953 (1994).

[37] J. P. Perdew, K. Burke, and M. Ernzerhof, Generalized gradient approximation made simple, Phys. Rev. Lett. **77**, 3865 (1996).

[38] S. Grimme, Semiempirical GGA-type density functional constructed with a long-range dispersion correction, J. Comput. Chem. **27**, 1787 (2006).

[39] V. Wang, N. Xu, J. C. Liu, G. Tang, and W. Geng, VASPKIT: A user-friendly interface facilitating high-throughput computing and analysis using VASP code, Comput. Phys. Commun. **267**, 108033 (2021).

[40] R. Jinnouchi, J. Lahnsteiner, F. Karsai, G. Kresse, and M. Bokdam, Phase transitions of hybrid perovskites simulated by machine-learning force fields trained on the fly with Bayesian inference, Phys. Rev. Lett. **122**, 225701 (2019).

[41] R. Jinnouchi, F. Karsai, and G. Kresse, On-the-fly machine learning force field generation: Application to melting points, Phys. Rev. B **100**, 014105 (2019).

[42] R. Jinnouchi, F. Karsai, C. Verdi, R. Asahi, and G. Kresse, Descriptors representing two- and three-body atomic distributions and their effects on the accuracy of machine-learned inter-atomic potentials, J. Chem. Phys. **152**, 234102 (2020).

[43] M. P. Allen and D. J. Tildesley, *Computer Simulation of Liquids* (Oxford University Press, Oxford, UK, 2017).

[44] X. Gonze and C. Lee, Dynamical matrices, Born effective charges, dielectric permittivity tensors, and interatomic force constants from density-functional perturbation theory, Phys. Rev. B **55**, 10355 (1997).

[45] A. Musaelian, S. Batzner, A. Johansson, L. Sun, C. J. Owen, M. Kornbluth, and B. Kozinsky, Learning local equivariant representations for large-scale atomistic dynamics, Nat. Commun. **14**, 579 (2023).

[46] H. Yu, S. Deng, M. Xie, Y. Zhang, X. Shi, J. Zhong, C. He, and H. Xiang, Switchable ferroelectricity in subnano silicon thin films, arXiv:2407.01914.

[47] A. P. Thompson, H. M. Aktulga, R. Berger, D. S. Bolintineanu, W. M. Brown, P. S. Crozier, P. J. in 't Veld, A. Kohlmeyer, S. G. Moore, T. D. Nguyen, R. Shan, M. J. Stevens, J. Tranchida, C. Trott, and S. J. Plimpton, LAMMPS - a flexible simulation tool for particle-based materials modeling at the atomic, meso, and continuum scales, Comput. Phys. Commun. **271**, 108171 (2022).

[48] S. Nosé, A unified formulation of the constant temperature molecular dynamics methods, J. Chem. Phys. **81**, 511 (1984).

[49] K. Levenberg, A method for the solution of certain non-linear problems in least squares, Q. Appl. Math. **2**, 164 (1944).

[50] D. W. Marquardt, An algorithm for least-squares estimation of nonlinear parameters, J. Soc. Ind. Appl. Math. **11**, 431 (1963).

[51] A. Weston, Y. Zou, V. Enaldiev, A. Summerfield, N. Clark, V. Zólyomi, A. Graham, C. Yelgel, S. Magorrian, M. Zhou, J. Zultak, D. Hopkinson, A. Barinov, T. H. Bointon, A. Kretinin, N. R. Wilson, P. H. Beton, V. I. Fal'ko, S. J. Haigh, and R. Gorbachev, Atomic reconstruction in twisted bilayers of transition metal dichalcogenides, Nat. Nanotechnol. **15**, 592 (2020).

[52] R. He, B. Zhang, H. Wang, L. Li, P. Tang, G. Bauer, and Z. Zhong, Ultrafast switching dynamics of the ferroelectric order in stacking-engineered ferroelectrics, Acta Mater. **262**, 119416 (2024).

[53] R. D. King-Smith and D. Vanderbilt, Theory of polarization of crystalline solids, Phys. Rev. B **47**, 1651 (1993).

[54] R. Resta, Theory of the electric polarization in crystals, Ferroelectrics **136**, 51 (1992).

[55] D. Bennett, G. Chaudhary, R.-J. Slager, E. Bousquet, and P. Ghosez, Polar meron-antimeron networks in strained and twisted bilayers, Nat. Commun. **14**, 1629 (2023).

[56] D. Bennett, W. J. Jankowski, G. Chaudhary, E. Kaxiras, and R.-J. Slager, Theory of polarization textures in crystal supercells, Phys. Rev. Res. **5**, 033216 (2023).

[57] J. Wang, X. Li, X. Ma, L. Chen, J.-M. Liu, C.-G. Duan, J. Íñiguez-González, D. Wu, and Y. Yang, Ultrafast switching of sliding polarization and dynamical magnetic field in van der Waals bilayers induced by light, Phys. Rev. Lett. **133**, 126801 (2024).

[58] T.-H.-Y. Vu, D. Bennett, G. N. Pallewella, M. H. Uddin, K. Xing, W. Zhao, S. H. Lee, Z. Mao, J. B. Muir, L. Jia, J. A. Davis, K. Watanabe, T. Taniguchi, S. Adam, P. Sharma, M. S. Fuhrer, and M. T. Edmonds, Imaging topological polar structures in marginally twisted 2D semiconductors, arXiv:2405.15126.

[59] F. Lou, X. Y. Li, J. Y. Ji, H. Y. Yu, J. S. Feng, X. G. Gong, and H. J. Xiang, PASP: Property analysis and simulation package for materials, J. Chem. Phys. **154**, 114103 (2021).

[60] S. Batzner, A. Musaelian, L. Sun, M. Geiger, J. P. Mailoa, M. Kornbluth, N. Molinari, T. E. Smidt, and B. Kozinsky, $E(3)$-equivariant graph neural networks for data-efficient and accurate interatomic potentials, Nat. Commun. **13**, 2453 (2022).

[61] J. Gasteiger, J. Groß, and S. Günnemann, Directional message passing for molecular graphs, in *Proceedings of the 8th International Conference on Learning Representations, ICLR 2020, Addis Ababa, Ethiopia, April 26–30, 2020* (OpenReview.net, 2020).

[62] R. Landauer, Electrostatic considerations in $BaTiO_3$ domain formation during polarization reversal, J. Appl. Phys. **28**, 227 (1957).

[63] B. Xu, V. Garcia, S. Fusil, M. Bibes, and L. Bellaiche, Intrinsic polarization switching mechanisms in $BiFeO_3$, Phys. Rev. B **95**, 104104 (2017).

[64] B. Xu, J. Íñiguez, and L. Bellaiche, Designing lead-free antiferroelectrics for energy storage, Nat. Commun. **8**, 15682 (2017).

[65] C. Daumont, W. Ren, I. C. Infante, S. Lisenkov, J. Allibe, C. Carrétéro, S. Fusil, E. Jacquet, T. Bouvet, F. Bouamrane, S. Prosandeev, G. Geneste, B. Dkhil, L. Bellaiche, A. Barthélémy, and M. Bibes, Strain dependence of polarization and piezoelectric response in epitaxial $BiFeO_3$ thin films, J. Phys.: Condens. Matter **24**, 162202 (2012).

[66] S. Lisenkov, D. Rahmedov, and L. Bellaiche, Electric-field-induced paths in multiferroic $BiFeO_3$ from atomistic simulations, Phys. Rev. Lett. **103**, 047204 (2009).

[67] C. Ke, F. Liu, and S. Liu, Superlubric motion of wave-like domain walls in sliding ferroelectrics, arXiv:2502.01007.